NiMo@C$_3$N$_5$ heterostructures with multiple electronic transmission channels for highly efficient hydrogen evolution from alkaline electrolytes and seawater

Xiuming Bu [a,1], Xiongyi Liang [a,1], Yu Bu [b,1], Quan Quan [a], You Meng [a], Zhengxun Lai [a], Wei Wang [a], Chuntai Liu [d], Jian Lu [b,c,e], Chi-Man Lawrence Wu [a,*], Johnny C. Ho [a,f,*]

[a] Department of Materials Science and Engineering, City University of Hong Kong, Hong Kong 999 077, PR China
[b] Centre for Advanced Structural Materials, City University of Hong Kong Shenzhen Research Institute, Shenzhen 518 057, PR China
[c] Department of Mechanical Engineering, City University of Hong Kong, Hong Kong 999 077, PR China
[d] Key Laboratory of Advanced Materials Processing & Mold (Zhengzhou University), Ministry of Education, Zhengzhou 450 002, PR China
[e] Centre for Advanced Structural Materials, City University of Hong Kong Shenzhen Research Institute, Greater Bay Joint Division, Shenyang National Laboratory for Materials Science, Shenzhen 518 057, PR China
[f] State Key Laboratory of Terahertz and Millimeter Waves, City University of Hong Kong, Hong Kong 999 077, PR China

ARTICLE INFO

ABSTRACT

Designing highly efficient and stable electrocatalysts for hydrogen evolution reaction (HER), particularly in seawater, still remains a challenging task. Herein, the unique heterostructures composed of 1D NiMo cores and 2D C$_3$N$_5$ shells (NiMo@C$_3$N$_5$) are rationally designed and demonstrated as the robust HER catalysts in both alkaline electrolytes and natural seawater, where the carbon-based shell can effectively protect the catalyst core from seawater poisoning. Based on the experimental investigation and density functional theory calculation, multiple electronic transmission channels were found to establish at the interface between NiMo cores and C$_3$N$_5$ shells, thus providing efficiently optimized HER pathways to achieve minimized overpotential with a reduced energy barrier of the rate-determining step. More importantly, the NiMo@C$_3$N$_5$ hybrids exhibit stable HER performance with a high Faradaic efficiency of 94.8% in seawater, which is superior to that of commercial Pt/C. All these results can evidently highlight a feasible strategy to develop high-performance HER electrocatalysts via interface engineering.

1. Introduction

Due to the high weight energy density and pollution-free characteristics, hydrogen is widely considered as a promising clean energy resource [1,2]. Among many recent developments, electrochemical water splitting powered by renewable-generated electricity provides an efficient means to produce high-purity green hydrogen through environmentally friendly processes [3–5]. Utilizing this green production scheme, the manufacturing cost and reliability of hydrogen are found highly dependent on the composition and corresponding electronic structure of electrocatalysts [6–8]. To date, Pt-dominated materials are employed as the best-performed electrocatalysts for hydrogen evolution reaction (HER) owing to their fast kinetics and excellent conductivities; however, the scarcity and high cost of Pt-based catalysts inevitably limit

their large-scale utilization [9,10]. Also, purified freshwater is usually required as the hydrogen feedstock in water splitting, where the usage of freshwater would certainly worsen the issue of global clean water shortage [12–14]. Fortunately, there is plenty of seawater resource available around the world. The green hydrogen extracted from seawater can be further processed to produce other chemical fuels, such as methane and methanol [15]. In this regard, it is of great scientific and practical significance to develop high-performance and cost-effective electrode materials for seawater splitting.

Generally, the design principles of electrocatalysts are rather different between conventional water splitting and seawater splitting. The presence of various dissolved ions, including Ca^{2+}, Mg^{2+} and Cl$^-$, and bacteria/microbes in seawater would easily poison the catalysts, deteriorating the durability of seawater splitting [11]. Even though

* Corresponding authors.
  E-mail addresses: apcmlwu@cityu.edu.hk (C.-M. Lawrence Wu), johnnyho@cityu.edu.hk (J.C. Ho).
  [1] Xiuming Bu, Xiongyi Liang and Yu Bu contributed equally to this work.

numerous efforts have been devoted to explore alternative Pt-free HER catalysts that are robust and compatible with seawater electrolytes, their catalyst performances are still far from acceptable owing to the poor stability and insufficient degree of water dissociation [16–18]. In fact, based on Sabatier's principle, the ideal HER catalysts should have the free adsorption energy of hydrogen atom (ΔG_{H*}) being close to zero; therefore, the catalysts can promote the efficient proton and electron transfer steps as well as the rapid hydrogen molecule release processes in order to enhance the electrocatalytic hydrogen production [19–23]. Apart from the Pt-based materials, the NiMo-based alloys are also found to have the value of ΔG_{H*} close to zero and other properties suitable to serve as an efficient HER catalyst [24–27]. Particularly, one-dimensional (1D) NiMo nanowires directly synthesized on Ni foams have just been demonstrated to exhibit HER performance even better than commercial Pt/C electrodes in 1 M KOH [28]. It is also proved that the insertion of a carbon-based shell layer would effectively protect the catalyst core from seawater poisoning and bacteria/microbes precipitation in order to retain the electrocatalytic stability [29,30]. For instance, the low-cost CoMoP nanocrystals could be coated with several layers of N-doped carbon shells by a simple one-step pyrolysis method, and can provide comparable electrocatalytic performance to Pt/C catalysts with Faraday efficiency of over 92.5% [30]. In this case, an appropriate carbon-based shell together with the NiMo core are expected to provide an efficient electrocatalyst for seawater splitting.

At the same time, there is a new kind of two-dimensional (2D) N-rich carbon nanomaterials, also known as C_3N_5, lately developed based on the graphitic carbon nitrides (g-C_3N_4) [31]. As illustrated by experimental results and theoretical calculations, this C_3N_5 material can serve as a promising protective shell layer for catalysts, especially that the high nitride content in C_3N_5 provides more catalytic active sites for reactions due to the asymmetric electron spin density and charge polarization between the carbon and nitride atoms [31,32]. Once C_3N_5 is integrated with specific transition metals (e.g. NiMo alloys), it is anticipated to have more electron transfer channels established on the strongly coupled nano-interfaces between C_3N_5 and NiMo because of the abundant N atoms and easily tailorable electronic states of Ni and Mo atoms, and would further optimize the resulting free energy for enhanced water splitting. Herein, the core–shell heterostructures composed of 1D NiMo cores and 2D C_3N_5 shells (NiMo@C_3N_5) are rationally designed and demonstrated as the robust HER catalysts in both alkaline electrolytes and natural seawater. Notably, this unique NiMo@C_3N_5 core–shell heterostructure can be easily synthesized via a scalable and low-cost chemical method, where the 1D@2D configuration is beneficial for forming abundant nano-interfaces, thus promoting the reaction kinetics of HER. It is impressive that the prepared NiMo@C_3N_5 electrocatalyst exhibits excellent HER performances with an overpotential of only 80 mV when the current density is 10 mA cm^{-2} with a mass loading of 0.554 mg cm^{-2} in 1 M KOH. Both experimental and density functional theory (DFT) results reveal that the Mo-N covalent bonds between NiMo and C_3N_5 nano-interfaces can efficiently speed up the sluggish HER kinetics with a significantly reduced energy barrier. More importantly, the NiMo@C_3N_5 catalyst shows a respectably high HER performance and stability in natural seawater, delivering the comparable current density to those of commercial Pt/C catalysts after a long-term stability test. All these findings can evidently indicate the practical potential of using NiMo@C_3N_5 core–shell heterostructure electrocatalysts for direct seawater splitting.

2. Materials and methods

2.1. Preparation of 2D C_3N_5 nanosheets

The 2D C_3N_5 nanosheets were prepared according to a previous report with minor modifications [31]. Typically, 5 g of melamine placed in an alumina crucible with a cover was heated at 425 °C for 12 h with a heating rate of 5 °C min^{-1}. After cooling to room temperature, the

resulting coarse powder particles were milled into fine powders and dispersed in distilled water under ultrasonication. Then, the dispersions were refluxed for several hours to remove the impurities. The resulted white product (melem) was collected and dried at 60 °C.

Next, 2 g of the white product (melem) was added into 25 mL of hydrazine hydrate solution (60 %), sealed within an autoclave, and heated at 140 °C for 24 h. After cooling to room temperature, the pH value of the solution was first carefully adjusted to 1–2 with the controlled addition of HCl (10 %) to remove any unreacted solids and re-precipitated at a pH value of 7–8 via adding NaOH (10 %) solution. Melem hydrazine was synthesized after repeating this process three times. Finally, C_3N_5 nanosheets were obtained by heating melem hydrazine at 550 °C for 2 h with a heating rate of 5 °C min^{-1} under Ar atmosphere.

2.2. Preparation of 1D NiMo nanorods

The preparation of NiMo alloy nanowires was according to our previous report. Specifically, 0.5 mmol Ni(NO$_3$)$_2$ and 0.5 mmol NaMoO$_4$ were added into 10 mL distilled water under magnetic stirring for 5 min to form a homogeneous solution. The mixture solution was transferred to a 15 mL stainless-steel Teflon-lined autoclave and heated at 160 °C for 6 h. The resulted precipitate (NiMoO$_4$ nanorods) was then washed with ethanol and DI water for several times and dried at 60 °C overnight. To prepare NiMo nanowires, the NiMoO$_4$ nanowires were treated at 550 °C for 1 h with a heating rate 5 °C/min under an Ar/H$_2$ (200/100 sccm) environment. After cooling down to the room temperature, H$_2$ was stopped and 10 sccm O$_2$ was provided for 30 min to passivate the sample.

2.3. Preparation of NiMo@C_3N_5 core–shell hybrids

In a typical process, a varied amount of melem hydrazine (i.e. 7, 10, 20 and 30 mg) and 50 mg of NiMo nanorods were added into 10 mL of ethanol under stirring for 30 min to obtain a uniform solution. Then, the precipitate (melem hydrazine/NiMo nanorods) was obtained after drying at 60 °C under vacuum overnight. Finally, NiMo@C_3N_5 hybrids were prepared via heating the melem hydrazine/NiMo nanorods at 550 °C for 2 h under Ar atmosphere. The obtained samples was named as NiMo@C_3N_5-7 mg, NiMo@C_3N_5-10 mg, NiMo@C_3N_5-20 mg and NiMo@C_3N_5-30 mg, respectively.

2.4. Preparation of NiMo/C_3N_5 mixtures

Apart from the NiMo@C_3N_5 core–shell hybrids, physically mixed NiMo/C_3N_5 mixtures are also prepared in this study. Various amounts of C_3N_5 (i.e. 7, 10 and 20 mg) and 50 mg of NiMo nanorods were added into 10 mL of ethanol solution, followed by stirring the mixture at 60 °C. The NiMo/C_3N_5 powder was then collected after drying the solution. The obtained samples were named as NiMo/C_3N_5-7 mg, NiMo/C_3N_5-10 mg and NiMo/C_3N_5-20 mg, respectively.

2.5. Material characterization

Powder X-ray diffraction (Bruker D2 Phaser, Billerica, MA, USA) was employed to investigate the crystalline structure of prepared samples in a 2θ scan ranging from 10° to 90° with a scanning rate of 0.05°/s, in which the machine is equipped with a monochromatized Cu–Kα radiation. Morphologies and elemental analysis of the samples were characterized via a field-emission scanning electron microscope (SEM, SU-8010, Hitachi, Tokyo, Japan) with an accelerating voltage of 15 kV and a high-resolution transmission electron microscope (HRTEM, Tecnai G^2 F30, FEI, Hillsboro, OR, USA) with an accelerating voltage of 300 kV. Brunauer-Emmett-Teller (BET) specific surface area and pore volume of the samples were assessed based on nitrogen adsorption isotherms using a NOVA 1200e gas adsorption apparatus (Quantachrome Instruments,

Boynton Beach, FL, USA). X-ray photoelectron spectroscopy (XPS, VG Multilab 2000, Thermo Fisher Scientific, Waltham, MA, USA) data were collected at an ultrahigh vacuum (2×10^{-6} Pa) environment with a monochromatic Al–Kα radiation. It should be noticed that all the binding energies were calibrated with C1s peak at 284.8 eV.
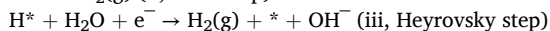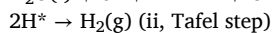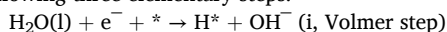
2.6. Electrochemical measurement

The electrochemical characterization was investigated with a Gamry 300 electrochemical workstation with a three-electrode system at room temperature. The working electrode was prepared as follows: 5 mg of electrocatalysts ultrasonically dispersed in a mixture containing 340 μL of ethanol, 100 μL of DI water and 20 of μL Nafion (5 wt%) for 2 h to prepare a homogeneous solution. Then, 10 μL of electrocatalyst dispersion was drop-casted onto a glassy carbon electrode (0.196 cm^2), where the mass loading was about 0.553 mg cm^{-2}. A carbon rod and a saturated Ag/AgCl electrode (protected by salt bridge) served as the counter electrode and reference electrode, respectively. All potentials in this work were referenced versus the reversible hydrogen electrode (RHE) by the equation of $E_{RHE} = E_{SCE} + (0.197 + 0.059 \times pH)$ V, where E_{RHE} is the potential referred to RHE and E_{SCE} is the measured potential against the saturated calomel electrode (SCE) reference electrode. The HER performance was collected in 1 M KOH (pH = 13.7) solution and natural seawater (collected near Tsuen Wan, Hong Kong, pH = 7.4) via linear sweep voltammetry (LSV) with a scan rate of 5 mV s^{-1}. Several cyclic voltammetry (CV) cycles were conducted before the test until the curves showed the unobvious change. Gas measurement was carried out by using gas chromatography (GC-7900, Techcomp Co.) with argon as the carrier gas. The measurement of H$_2$ volume was performed in an airtight H shape cell. Before testing, high purity N$_2$ was introduced for 1 h. The electrocatalysis process was carried out with a constant current of 10 mA in the natural seawater.

2.7. Computational details

All the first principle calculations were performed using spin-polarized DFT as implemented in Quantum Espresso [33,34]. Generalized gradient approximation (GGA) with Perdew-Burke-Ernzerhof (PBE) functional was selected to describe the exchange–correlation interaction [35]. The zero-damping DFT-D3 method of Grimme was introduced to calculate the van der Waals corrections [36]. A plane-wave cutoff of 50 Ry and a density cutoff of 500 Ry were used based on standard solid-state pseudopotentials with projector augmented wave (PAW) method [37,38]. A five layers slabs of NiMo and NiMo@C$_3$N$_5$ with a sufficiently vacuum slab of 15 Å was built, where two bottom layers are fixed. For sampling the Brillouin zone, Gamma point was set. All atoms were fully relaxed until the forces on each atom were less than 0.02 eV/Å.

The calculation of Gibbs free energy change (ΔG) for each elemental step was based on the computational hydrogen electrode (CHE) model [39], which can be expressed by $\Delta G = \Delta E + \Delta E_{ZPE} - T\Delta S$, where ΔE is the electronic energy difference between the free standing and adsorption states of reaction intermediates; ΔE_{ZPE} and ΔS are the changes in zero point energies and entropy, respectively, which are obtained from the vibrational frequency calculations. T is the temperature, and is set to be 298.15 K in this work. H$_2$ and H$_2$O were used as the reference states. The complete HER catalytic process in alkaline condition includes the following three elementary steps:

$H_2O(l) + e^- + * \rightarrow H* + OH^-$ (i, Volmer step)

$2H* \rightarrow H_2(g)$ (ii, Tafel step)

$H* + H_2O + e^- \rightarrow H_2(g) + * + OH^-$ (iii, Heyrovsky step)

where * indicates the adsorption site. Based on previous reports, good balance between the adsorption of catalyst surface between H* and OH* indicates a good catalyst for HER in alkaline condition [40,41]. In addition, the nudged elastic band method (NEB) was used to search the transition states and calculate the reaction barriers [42,43]. All the reaction barriers combined with the Gibbs free energy states were calculated.

3. Results and discussion

3.1. Characterization of NiMo@C$_3$N$_5$ and NiMo/C$_3$N$_5$

As shown in the schematic diagram in Fig. 1a, the preparation process of NiMo@C$_3$N$_5$ core–shell nanostructures is presented. Typically, 1D NiMo nanorods were first prepared by hydrothermally reacting Ni (NO$_3$)$_2$ and NaMoO$_4$, and then reduction based on our previous reports (Fig. S1, Supporting Information) [28]. In order to obtain the intense contact between NiMo nanorods and C$_3$N$_5$ nanosheets, the C$_3$N$_5$ precursor (melem hydrazine) was mixed with NiMo nanorods in ethanol solution under stirring on a hotplate. After drying, the resulting powder was converted into NiMo@C$_3$N$_5$ electrocatalysts under Ar atmosphere (Fig. 1b and Fig. S2, Supporting Information). The X-ray diffraction (XRD) technique was first employed to investigate the composition and crystal structure of the obtained hybrids. As demonstrated in Fig. S3 in the Supporting Information, the main peaks of NiMo nanorods arise mainly from NiMo (JCPDS 65–5480) in the XRD spectrum, with very small amounts of pure Mo (JCPDS 80–2855) also detected. It should also be noticed that our previous report had shown the NiMo nanorods prepared at an optimal temperature of 550 °C exhibiting the best HER performance [28]. After forming the hybrids with C$_3$N$_5$, the changes in the crystal structure of NiMo are negligible. Moreover, in contrast with the XRD pattern of pure C$_3$N$_5$ (Fig. S4, Supporting Information), there is not any (0 0 2) peak found on the NiMo@C$_3$N$_5$ hybrids, indicating no formation of the bulk C$_3$N$_5$ phase [31]. In fact, after the in-situ coating of C$_3$N$_5$ layers onto NiMo nanorods, the obtained NiMo@C$_3$N$_5$ hybrids exhibit the core–shell nanorod configuration, in which a low crystalline layer (~2 nm thick) is observed to wrap around the nanorod surface. As compared with the pristine NiMo nanorods with high crystallinity (Fig. S1, supporting information), a porous layer is witnessed on the NiMo@C$_3$N$_5$ surface when the hybrid is exposed to electron beam irradiation as illustrated in Fig. 1c. A similar phenomenon is also occurred on the single C$_3$N$_5$ layer, which can be attributed to the surface electron accumulation (Fig. S5, Supporting Information). Therefore, the porous surface layer of the hybrid can be determined as C$_3$N$_5$. Also, the lattice fringes of the partially exposed NiMo core are observed with lattice spacings of 0.37 nm and 0.27 nm, which can be assigned to the (1 1 3) and (1 2 1) planes of orthorhombic NiMo, respectively, indicating again the crystallinity of NiMo got retained after the shell layer deposition. Elemental mappings of Ni, Mo, C and N are as well corresponded well to the different constituent profiles of NiMo@C$_3$N$_5$ (Fig. 2e-i). All these results reveal clearly the successful preparation of the NiMo@C$_3$N$_5$ core–shell heterostructure.

To shed light on the effect of strong electron interaction within NiMo@C$_3$N$_5$ hybrids on their electrocatalytic performance, the physically mixed NiMo and C$_3$N$_5$ mixture, labelled as NiMo/C$_3$N$_5$, are also prepared in addition to the NiMo@C$_3$N$_5$ core–shell heterostructure. The SEM image and corresponding EDS mappings of NiMo/C$_3$N$_5$ are first shown in Fig. S6, Supporting Information, with the preparation procedure described in the materials and methods section. Fourier transform infrared (FTIR) spectroscopy was then utilized to investigate the functional groups of different materials. As depicted in the spectra in Fig. 2a, there are IR bands located at 1411 and 1595 cm^{-1}, which are attributed to the C-N stretching of heptazine (C$_6$N$_7$) aromatic nucleus, confirming the successful preparation of C$_3$N$_5$ [31]. Furthermore, the IR bands at 688, 798, 880 and 944 cm^{-1} are ascribed to the metal-O-metal vibration [44]. As compared with the pristine NiMo nanorods and C$_3$N$_5$ nanosheets, there are obvious characteristic peaks located at 688, 798, 880, 944 and 1595 cm^{-1} for the NiMo/C$_3$N$_5$ mixture, suggesting the effective physical combination between NiMo and C$_3$N$_5$. It is interesting that the characteristic peak intensity of NiMo@C$_3$N$_5$ is found significantly reduced. This intensity reduction can be due to the strong electronic interaction influencing the original vibration mode.
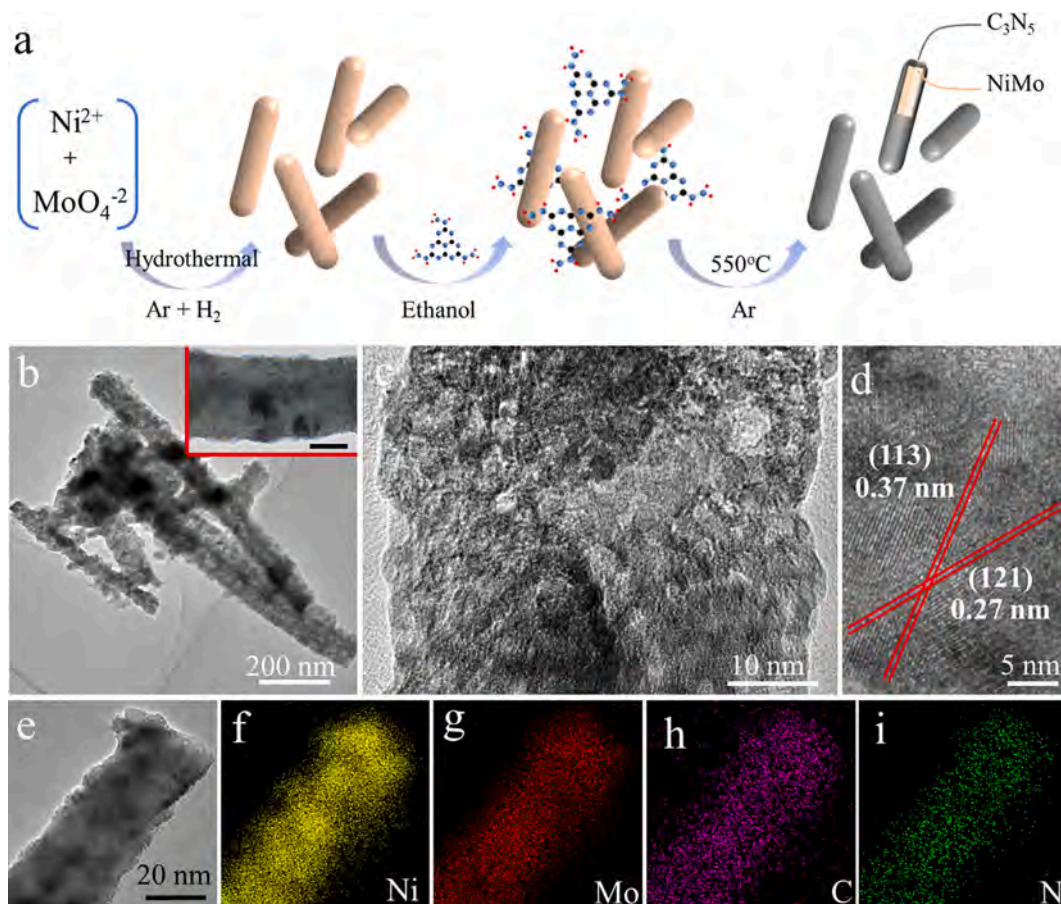
Fig. 1. (a) The schematic illustration of the preparation of NiMo@C$_3$N$_5$ electrocatalysts. (b) is the TEM image of NiMo@C$_3$N$_5$; c) and d) are the corresponding HRTEM images; (e-i) are the TEM image and the corresponding elemental mappings, including Ni, Mo, C and N.

Simultaneously, the specific surface area of different materials is characterized by Brunauer-Emmett-Teller (BET) analysis as shown in Fig. 2b. The C$_3$N$_5$ nanosheets reveal the largest specific surface area of 22.37 m^2·g^{-1} while the NiMo nanorods have the smallest specific surface area of 1.99 m^2·g^{-1}. The NiMo/C$_3$N$_5$ mixture and NiMo@C$_3$N$_5$ core–shell hybrids exhibit the similar specific surface area of 7.09 and 6.37 m^2·g^{-1}, respectively. These observations point toward that the introduction of C$_3$N$_5$ enhances the surface area of the catalyst, which is beneficial for promoting the efficient contact between catalysts and electrolytes. X-ray photoelectron spectroscopy (XPS) was next employed to evaluate the surface chemical composition and oxidation states of the NiMo/C$_3$N$_5$ and NiMo@C$_3$N$_5$ samples. The survey XPS spectra disclose that both NiMo/C$_3$N$_5$ and NiMo@C$_3$N$_5$ samples consist of the Ni, Mo, C and N elements (Fig. S7, Supporting Information). For the high-resolution spectra of N 1 s, the peak positions are almost the same between NiMo/C$_3$N$_5$ mixtures and pristine C$_3$N$_5$ nanosheets, but there is an obvious blue shift (~0.6 eV) of the bonding energy observed for NiMo@C$_3$N$_5$ hybrids, illustrating the substantial increase of electron density around the N constituent there (Fig. 2c). On the other hand, three are two main characteristic peaks located at 230.8 and 233.9 eV for the NiMo nanorods, which can be ascribed to signals of Mo 3d$_{5/2}$ and Mo 3d$_{3/2}$, respectively (Fig. 2d). No obvious chemical valence changes and binding energy shift of Mo 3d signals are observed for the NiMo/C$_3$N$_5$ mixture. For the NiMo@C$_3$N$_5$ core–shell heterostructure, the Mo 3d peaks shift to the higher binding energies by ~ 1.2 eV, suggesting that there is a change in the electron density. In addition, an extra peak appeared at 229.3 eV for the NiMo@C$_3$N$_5$ core–shell hybrid, attributable to the Mo-N bonding and being in good agreement with the previous reports [45]. The existence of this Mo-N covalent bond in the

NiMo@C$_3$N$_5$ hybrid clearly demonstrates the successful establishment of electron transfer channels. For the high-resolution spectra of Ni 2p, there are two dominant peaks positioned at 854.5 and 860.7 eV, which can be corresponded to Ni 2p$_{3/2}$ and its satellite peak, respectively (Fig. 2e) [46]. By analyzing the Ni 2p$_{3/2}$ peaks of all these samples, it is found that the Ni^{3+}/Ni^{2+} ratio of the NiMo@C$_3$N$_5$ hybrids increases significantly as compared to that of the NiMo/C$_3$N$_5$ mixture. Moreover, the Ni 2p peaks of the NiMo@C$_3$N$_5$ hybrids also shifts to the higher binding energy by ~ 0.8 eV, designating a decreased electron density around the Ni atom and being in an agreement with the witnessed Ni^{3+}/Ni^{2+} ratio change. These results are mostly attributed to the strong electronic coupling between NiMo and C$_3$N$_5$, where considerable amounts of electrons are transferred from the NiMo core to the C$_3$N$_5$ shell. Such strong electronic interaction is anticipated to improve the electrocatalytic activity of NiMo@C$_3$N$_5$ catalysts as demonstrated already for other hybrid catalyst systems [47–49].

3.2. Hydrogen evolution reaction performance in 1 M KOH

The electrochemical HER activities of the prepared catalysts were then accessed in 1 M KOH (pH = 13.67) with a standard three-electrode system. Before comparing the catalyst performance of different samples, the optimized NiMo@C$_3$N$_5$ and NiMo/C$_3$N$_5$ electrocatalysts have been prepared by varying their mass ratios between NiMo and C$_3$N$_5$ for the best electrochemical performance (Fig. S8 and S9, Supporting Information). Fig. 3a shows the IR corrected polarization curves of the optimized NiMo@C$_3$N$_5$ and NiMo/C$_3$N$_5$ electrodes together with the C$_3$N$_5$, NiMo and commercial Pt/C electrodes for comparison. The pristine C$_3$N$_5$ nanosheets show the negligible electrocatalytic activity while
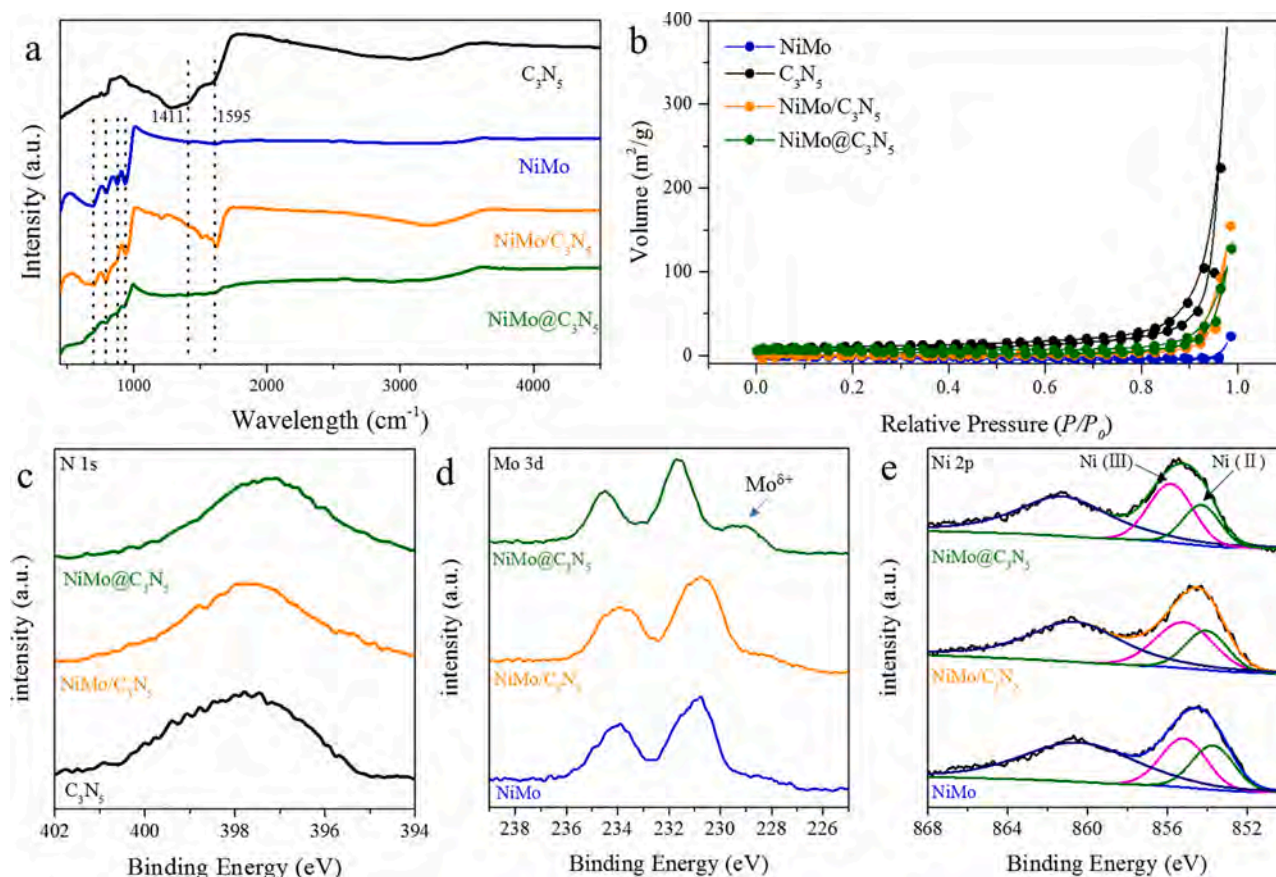
Fig. 2. (a) FTIR and (b) BET curves of C_3N_5, NiMo, NiMo@C_3N_5 and NiMo/C_3N_5, respectively. (c-e) XPS spectra of the different samples, including N 1 s, Mo 3d and Ni 2p signals.

NiMo nanorods exhibit good activity with an overpotential of 220 mV for a current density of 10 mA cm^{-2}. After integrating the NiMo nanorods with C_3N_5 nanosheets, the NiMo@C_3N_5 core–shell hybrids achieve an impressively low overpotential of 81 mV at 10 mA cm^{-2}, which is substantially lower than one of the NiMo/C_3N_5 mixtures (126 mV at 10 mA cm^{-2}). Importantly, the electrocatalytic performance of NiMo@C_3N_5 core–shell hybrids is even closer to that of commercial Pt/C catalyst. At the same time, the Tafel slopes derived from polarization curves were obtained to evaluate the electron transfer kinetics of catalysts for the HER process [50]. As shown in Fig. 3b, the fitted Tafel slope of NiMo@C_3N_5 is found as 68.3 mV dec^{-1}, which is smaller than those of NiMo (162.4 mV dec^{-1}), C_3N_5 (100.2 mV dec^{-1}) and NiMo/C_3N_5 (87.1 mV dec^{-1}), indicating a fast electron transfer process there. It is worth mentioning that the Tafel slopes of NiMo nanorods is observed as 162.4 mV dec^{-1}, which is larger than 120 mV dec^{-1}, denoting the HER kinetic process mostly governed by the water dissociation here (i.e. Volmer-Tafel mechanism) [51]. In contrast, the Tafel slope of NiMo@C_3N_5 hybrids and NiMo/C_3N_5 mixtures fall into the range of 40 ~ 120 mV dec^{-1}. The obvious Tafel slope change proves the introduction of C_3N_5 nanosheets to optimize the kinetic HER process of NiMo nanorods, thus improving their electrochemical activities. These results also indicate that the NiMo@C_3N_5 core–shell hybrids are the earth-abundant and efficient HER catalysts, being superior to most, if not all, recently reported high-performance electrocatalysts (Fig. 3c and also see the comparison in Table S1, Supporting information). In addition, the electrochemical impedance spectroscopy (EIS) is further employed to investigate the charge transfer ability in the interface between catalyst surface and electrolyte (Fig. 3d) [52]. The Nyquist plots revealed that the charge-transfer resistance of NiMo@C_3N_5 hybrids is apparently smaller than those of NiMo nanorods and NiMo/C_3N_5 mixtures, suggesting that NiMo@C_3N_5 possesses a faster charge-transfer capacity

during the HER process. The highly conductive surface and strong electron interaction of NiMo@C_3N_5 ensure its minimum charge-transfer resistance, leading to a fast electron transfer rate at the electrode/electrolyte interface. Moreover, to investigate the electrochemical surface area (ECSA) of catalysts, a simple cyclic voltammetry method was carried out to determine their values of double-layer capacitance, which is linearly proportional to the ECSA [53]. Fig. 3e illustrates the plots of different current density ($\Delta j = j_a$-j_c at -0.835 V vs RHE) against the scan rate (cyclic voltammogram (CV) curves shown in Fig. S10, Supporting Information). The NiMo@C_3N_5 core–shell hybrids possess the largest ECSA value (14.6 mF cm^{-2}), which is nearly 2 and 28 times larger than those of NiMo/C_3N_5 mixtures (6.9 mF cm^{-2}) and NiMo nanorods (0.5 mF cm^{-2}), respectively. Notably, the NiMo/C_3N_5 mixtures and NiMo@C_3N_5 hybrids have the similar BET area; hence, the higher ECSA value of NiMo@C_3N_5 suggests that the strong electron coupling improves the intrinsic activity of single active sites. The excellent electrochemical performance of NiMo@C_3N_5 can be attributed to the synergistic effect from its two components. In the NiMo@C_3N_5 system where the 2D C_3N_5 nanosheets wrap tightly on the NiMo nanorod surface, the C_3N_5 nanosheets do not only prevent the NiMo nanorods from aggregating and thus maximize the exposed active sites numbers, but also enhance the intense electron coupling effect between the C_3N_5 and NiMo, resulting in the increased activity of a single active site. To further evaluate the electrochemical stability of prepared NiMo@C_3N_5 electrodes, the long-term CV cycling tests and chronoamperometric response tests were carried out. As depicted in Fig. 3f, the NiMo@C_3N_5 electrode exhibits an insignificant degradation of current density after 1000 CV cycles and a long period of 10 h test, confirming the superior stability of NiMo@C_3N_5 for HER process under alkaline condition.
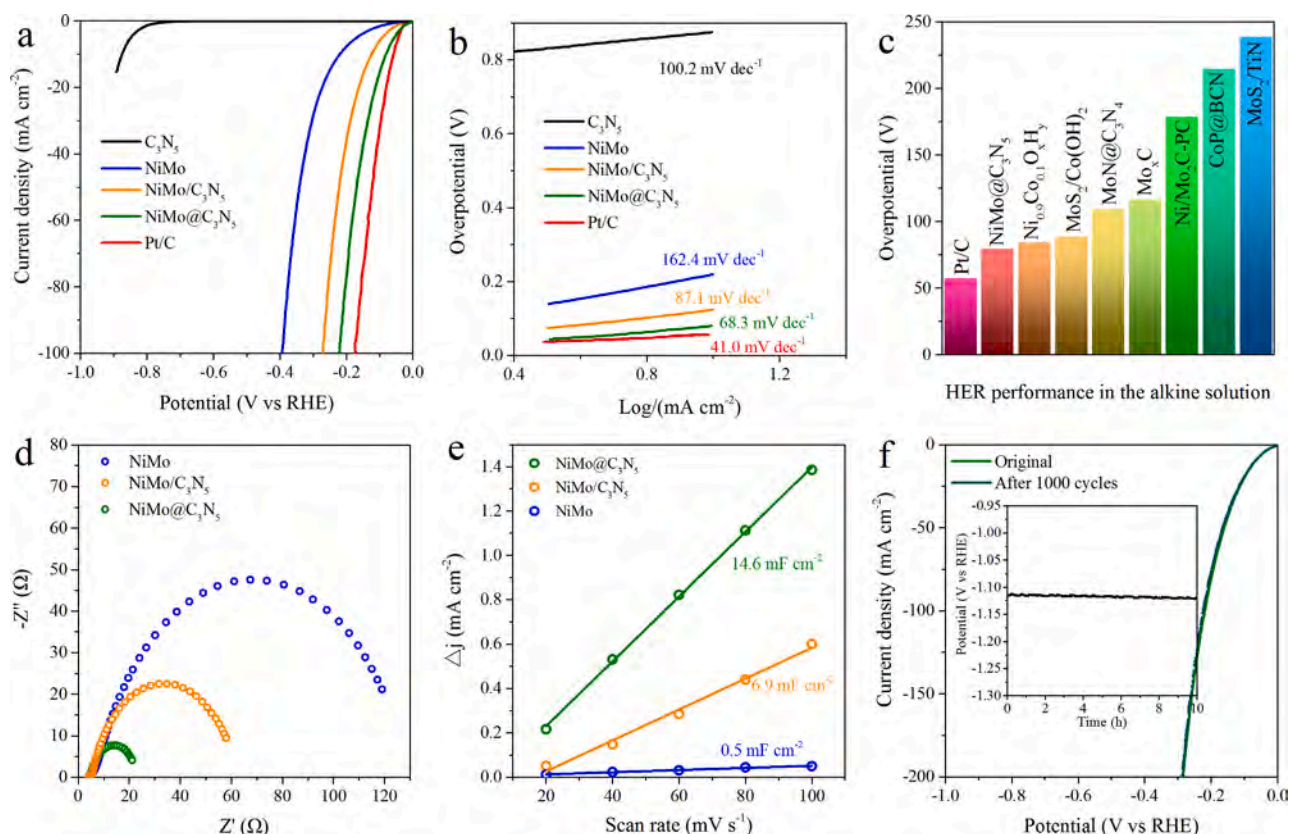
Fig. 3. (a) Polarization curves and (b) corresponding Tafel slopes of different samples measured in 1 M KOH at a scan rate of 5 mV s^{-1}. The samples include C$_3$N$_5$, NiMo, NiMo@C$_3$N$_5$, NiMo/C$_3$N$_5$ and Pt/C. (c) Comparison of the overpotential among others recently reported in the literature for the same current density of 10 mA cm^{-2}. The detailed comparison is also compiled in Table S1, Supporting Information. (d) Nyquist plots at the overpotential of 100 mV and (e) calculated double layer capacitance (C$_{dl}$) values of NiMo, NiMo@C$_3$N$_5$ and NiMo/C$_3$N$_5$, respectively. (f) Polarization curves before and after 1000 cycles with the inset showing the chronopotentiometry curve of NiMo@C$_3$N$_5$ at a constant current density of 10 mA cm^{-2} (without iR compensation).

3.3. Activity origin

In order to obtain deeper insight into the synergistic effects of NiMo@C$_3$N$_5$ hybrids on the HER activity, density functional theory (DFT) calculations were performed to investigate the key reaction steps of HER on the NiMo@C$_3$N$_5$ hybrid, compared with the NiMo. Specifically, the key elementary step, including water adsorption/dissociation, and the consequently generated adsorbed hydrogen (*H) on NiMo and NiMo@C$_3$N$_5$ surface in alkaline condition were considered. The optimized structures of water adsorption/dissociation and the *H adsorption of the electrocatalysts are shown in Fig. 4a and Fig. S11. Transition states (TS) of water splitting were searched by NEB method and all of the reaction barriers (ΔG_b) combined with Gibbs free energy correction are shown in Fig. 4b. Our theoretical investigation reveals that the initial water dissociation process is the rate-determining step (RDS). The water dissociation to *H and *OH on NiMo surface requires to overcome a high energy barrier of 0.96 eV, resulting in sluggish HER kinetics. On the contrary, the energy barrier for NiMo@C$_3$N$_5$ surface is reduced to 0.82 eV, suggesting that the introduction of C$_3$N$_5$ nanosheets can accelerate the kinetics of the water dissociation step [54,55]. The acceleration of water splitting on the NiMo@C$_3$N$_5$ surface owing to more negative water adsorption energy (-0.39 eV) there, hence leading to the stronger activation for water molecule and the smaller decomposition energy barrier. The adsorption free energy of hydrogen atom is also a critical descriptor to evaluate the hydrogen removal step of HER. As shown in Fig. 4b, calculated ΔG_{*H} value for NiMo and NiMo@C$_3$N$_5$ are −0.08 and −0.13 eV, respectively, which are closed to 0 eV. This indicates that hydrogen adsorption and release processes are efficient on the NiMo and NiMo@C$_3$N$_5$ surfaces.

It is believed that the origin of synergistic effect for NiMo@C$_3$N$_5$ surface derived from the electron redistribution between NiMo and C$_3$N$_5$ nano-interface. The projected density of states (PDOS), as well as the d-band center for NiMo and NiMo@C$_3$N$_5$ surfaces were calculated and shown in Fig. 4c. Compared with NiMo (-1.45 eV), the calculated d-band center for NiMo@C$_3$N$_5$ upshifted to −1.38 eV, which enhances the bonding strength between adsorbates and adsorbents, and finally promotes the H$_2$O dissociation step [56]. Based on the electron density difference analysis (Fig. S12), the obvious electron transfer from the NiMo core to the C$_3$N$_5$ shell can be observed and then leads to the electron redistribution at the nano-interface, which agrees well with the XPS results. In addition, Löwdin charge analysis shows that NiMo core donates a number of electrons of 1.65 e. Therefore, the theoretical results reveals that the introduction of C$_3$N$_5$ shell to NiMo core can optimizes the electronic structures of catalyst surfaces, thus promote kinetics of the rate-determining step.

3.4. Hydrogen evolution reaction performance in seawater

Because of the unique carbon-coated core–shell catalyst structure and the excellent electrocatalytic performance under alkaline condition, these NiMo@C$_3$N$_5$ hybrids are also employed as the HER catalyst in natural seawater (collected near Tsuen Wan, Hong Kong, pH = 7.4). As depicted in Fig. 5a to 5c, with increasing testing cycle, the electrocatalytic performance of NiMo@C$_3$N$_5$ declines slightly while that of commercial Pt/C decreases substantially. Specifically, the overpotential of NiMo@C$_3$N$_5$ is observed to be 486, 554 and 571 mV for the 1st, 10th and 30th cycle for the same current density of 10 mA cm^{-2}, respectively. For comparison, the corresponding overpotential of commercial Pt/C is
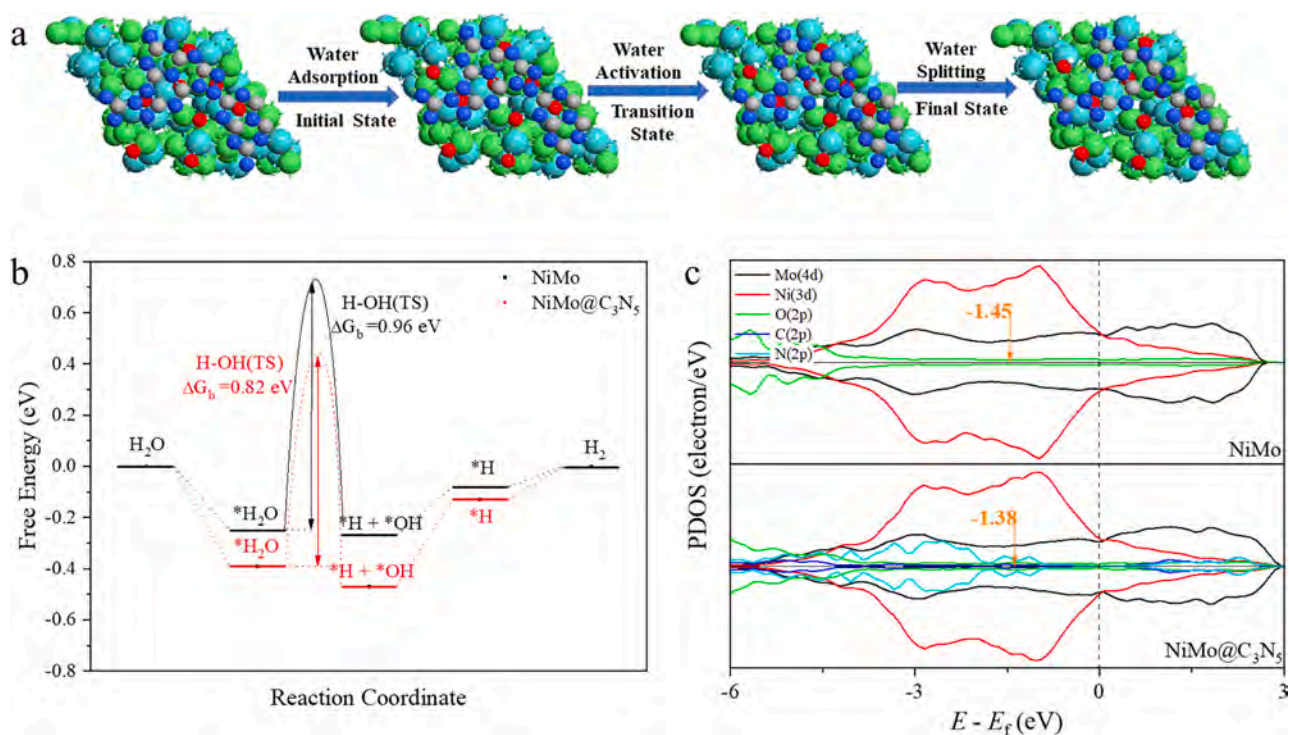
Fig. 4. (a) The optimized structures of H_2O dissociation on the NiMo@C_3N_5 surface. The green, cyan, red, blue, grey and white balls represent Ni, Mo, O, C, N, H atoms, respectively. (b) The free-energy diagram for the HER on NiMo and NiMo@C_3N_5 surfaces. (c) The projected density of states of NiMo and NiMo@C_3N_5 surfaces with aligned Fermi level.
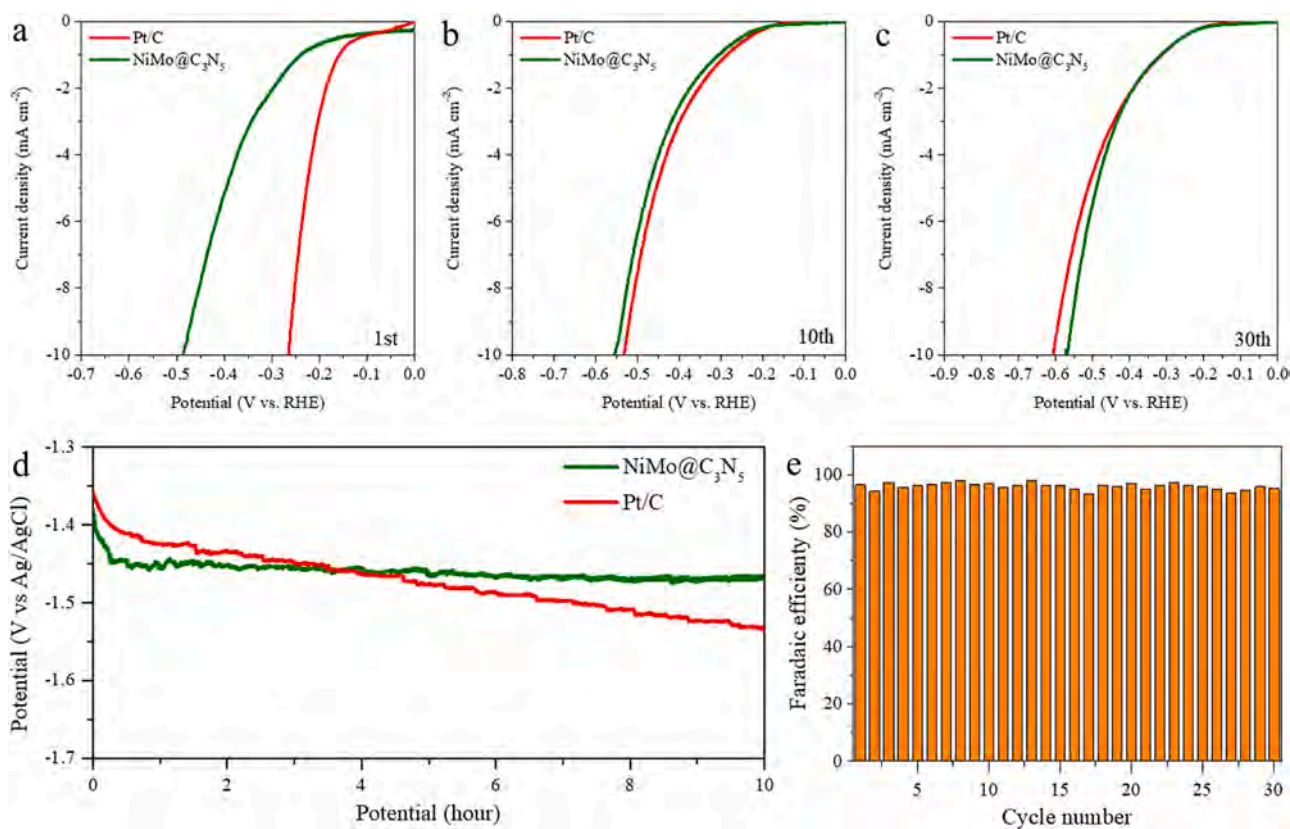

Fig. 5. (a-c) Polarization curves of NiMo@C_3N_5 and Pt/C in natural seawater at a scan rate of 5 mV s^{-1} for the 1st, 10th and 30th cycle of testing. (d) Time-dependent current density curve of NiMo@C_3N_5 and Pt/C, respectively. (e) Faradaic efficiency of different cycles of testing with a current density of 10 mA cm^{-2}.

found to be 264, 532 and 606 mV, accordingly. Furthermore, the long-term stability of the catalysts was evaluated with chronoamperometric (i-t) measurements for 10 h as shown in Fig. 5d. The NiMo@C_3N_5 core–shell hybrids demonstrate the enhanced stability (with only a voltage drop of 1.4%) than the commercial Pt/C catalyst. As contrasted with Pt/C, the C_3N_5 shells are anticipated to tightly wrap around the NiMo nanorods to protect the catalyst from the corrosion and poison of chemicals and biological impurities in the seawater. The Faradaic efficiency of the hybrid is measured to be nearly 94.8% in the natural seawater (Fig. S13, Supporting Information). After the successive 30 cycling test, there is not any noticeable variation observed for the Faradaic efficiency (Fig. 5e). The excellent electrochemical stability of NiMo@C_3N_5 can be attributed to the optimal design of the core–shell structure, in which NiMo nanorods are tightly wrapped by C_3N_5 nanolayers and the active sites are located at the interface. When the surface of NiMo@C_3N_5 is covered with the salt, the C_3N_5 acts as a buffer layer [11]. This way, the electrochemical reaction can still occur in the interface of NiMo@C3N5 system since the electrolyte species are capable of penetrating into the interface via capillary force or osmotic pressure. On the other hand, the commercial Pt/C is a physical mixture. Once the Pt directly interacts with the salt during the reaction, the active sites would be blocked, resulting in a significant decrease in the electrochemical performance.

To further understand the seawater electrolysis process, more physical characterizations were systematically employed. It should be noted that, contrary to the seawater electrolysis process usually performed under different stirring conditions, the following experiments were performed without any stirring, which can provide a direct observation of the practical effect of using natural seawater as electrolytes. As illustrated in Fig. 6a, before the seawater electrolysis test, the catalyst materials were evenly coated on the glassy carbon electrode, showing a smooth and clean surface. During the electrolysis process, the salt in the seawater is kept depositing on the electrode surface (Fig. 6b). Most of the deposited salt would peel off from the electrode surface because of gravity, while a small part of it got physically adsorbed on the catalyst surface as witnessed in the front-view and side-view images of the electrolysis cell (Fig. 6c and 6d). In this case, after the 10 h performance stability test, white particles were observed on the electrode surface, which obviously reduces the contact area between catalysts and electrolytes, thus decreasing the HER performance here. The corresponding EDS profile show that in addition to the constituent elements contained in the catalyst itself (i.e. Ni, Mo, C and N), there are other elements, which include Na, Mg, Cl and Ca (Fig. 6e). The SEM images further provide a clear evidence of the white particle mixture coated onto the NiMo@C_3N_5 electrocatalyst after seawater electrolysis (Fig. 6f and 6g), and the corresponding EDS mapping results is consistent with the EDS profiles (Fig. 6h-6n). As a result, the chemical composition of the white particles can be associated with $Mg(OH)_2$ and $Ca(OH)_2$. The existence of Na and Cl is mainly attributed to the physical adsorption of cations and anions, dissolved in seawater, onto the electrocatalysts, which is perfectly consistent with the previous reports [9].

4. Conclusion

In summary, based on the complementary experimental and theoretical investigation, the NiMo@C_3N_5 core–shell hybrids are demonstrated to function as a low-cost, highly-efficient and stable HER electrocatalyst in both alkaline condition and seawater. Impressively, the core–shell hybrids exhibit an overpotential of 81 mV at 10 mA cm^{-2} and a Tafel slope of 68.3 mV dec^{-1} in 1 M KOH. It was observed that the
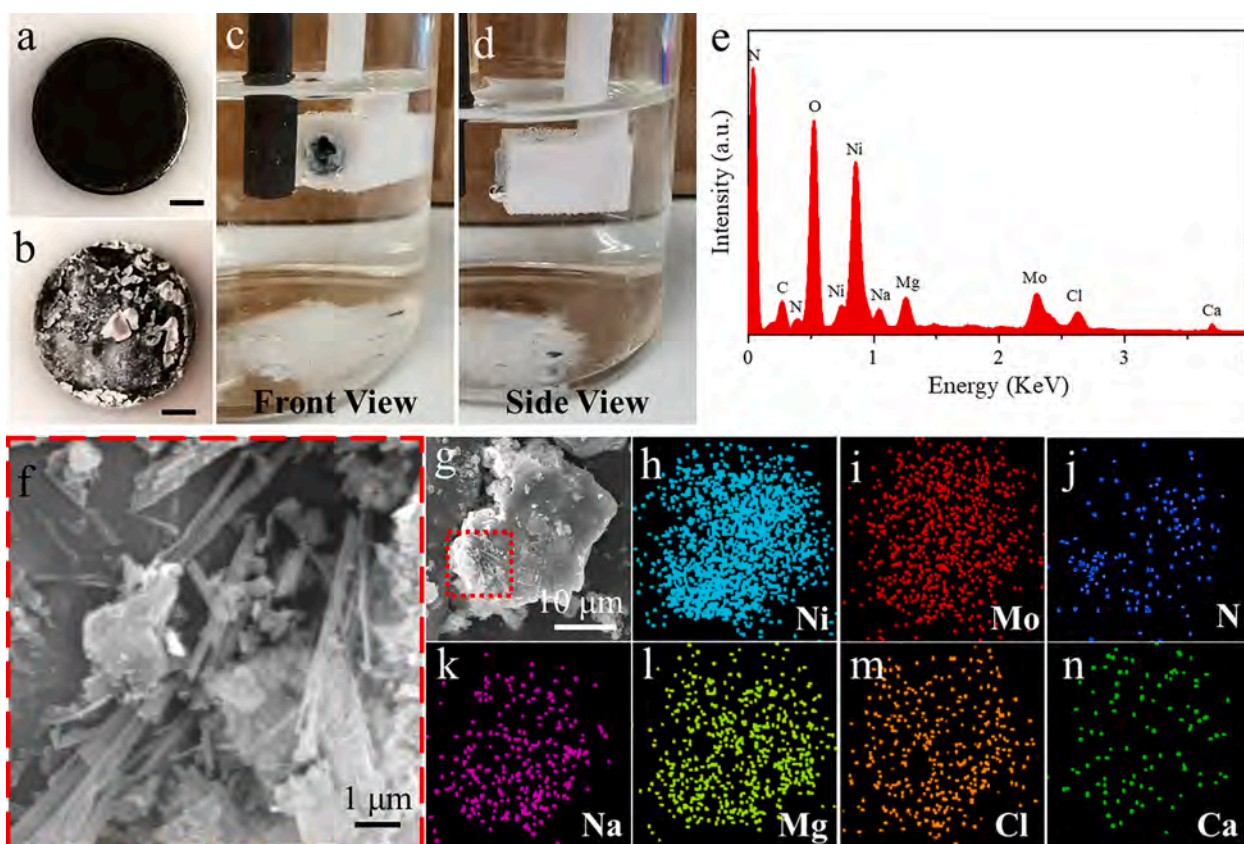

Fig. 6. (a, b) Optical images of the NiMo@C_3N_5 electrocatalyst deposited on the glassy carbon electrode before and after the seawater electrolysis. (c) Front-view and (d) side-view images of the glassy carbon electrode in the three-electrode system. (e) illustrates the EDS profile of the electrocatalyst after seawater electrolysis. (f, g) SEM image of the NiMo@C_3N_5 electrocatalyst after seawater electrolysis and (h-n) show the corresponding EDS mapping images. (f) The enlarged view of the area marked with red in (g).

electron redistribution effect induced by intense electron coupling between the NiMo core and the C_3N_5 shell optimized the HER reaction pathway, reducing the energy barrier of water dissociation step. More importantly, due to the C_3N_5-coated core–shell structure, the NiMo@C_3N_5 catalyst shows a respectably high HER performance and stability in the natural seawater, delivering a comparable current density to the one of commercial Pt/C catalyst after a long-term stability test. All these results evidently indicate the potential practical applications of NiMo@C_3N_5 core–shell hybrids in the direct seawater splitting.

Declaration of Competing Interest

The authors declare that they have no known competing financial interests or personal relationships that could have appeared to influence the work reported in this paper.

Acknowledgment

Appendix A. Supplementary data

Supplementary data to this article can be found online at https://doi.org/10.1016/j.cej.2022.135379.

References

[1] J.A. Turner, Sustainable Hydrogen Production Processes, Science. 305 (5686) (2004) 972–974.

[2] X. Zou, Y.u. Zhang, Noble metal-free hydrogen evolution catalysts for water splitting, Chem. Soc. Rev. 44 (15) (2015) 5148–5180.

[3] C. Liu, G. Zhang, L. Yu, J. Qu, H. Liu, Oxygen Doping to Optimize Atomic Hydrogen Binding Energy on NiCoP for Highly Efficient Hydrogen Evolution, Small. 1800421 (2018) 1–9.

[4] F. Tian, S. Geng, L. He, Y. Huang, A. Fauzi, W. Yang, Y. Liu, Y. Yu, Interface engineering: PSS-PPy wrapping amorphous Ni-Co-P for enhancing neutral-pH hydrogen evolution reaction performance, Chem. Eng. J. 417 (2021) 129232–129240.

[5] W. Yang, S. Chen, Recent progress in electrode fabrication for electrocatalytic hydrogen evolution reaction: A mini review, Chem. Eng. J. 393 (2020) 124726–124740.

[6] Z.W. She, J. Kibsgaard, C.F. Dickens, I. Chorkendorff, J.K. Nørskov, T.F. Jaramillo, Combining theory and experiment in electrocatalysis: Insights into materials design, Science. 355 (2017), https://doi.org/10.1126/science.

[7] F. Yang, T. Xiong, P. Huang, S. Zhou, Q. Tan, H. Yang, Y. Huang, M.S. Jie, T. Balogun, Nanostructured transition metal compounds coated 3D porous core-shell carbon fiber as monolith water splitting electrocatalysts: A general strategy, Chem. Eng. J. 423 (2021) 130279.

[8] X. Lu, K. hang Ye, S. Zhang, J. Zhang, J. Yang, Y. Huang, H. Ji, Amorphous type FeOOH modified defective BiVO4 photoanodes for photoelectrochemical water oxidation, Chem. Eng. J. 428 (2022) 131027.

[9] N. Mahmood, Y. Yao, J.W. Zhang, L. Pan, X. Zhang, J.J. Zou, Electrocatalysts for Hydrogen Evolution in Alkaline Electrolytes: Mechanisms, Challenges, and Prospective Solutions, Adv. Sci. 5 (2018) 1700464–1700487.

[10] F. Song, L. Bai, A. Moysiadou, S. Lee, C. Hu, L. Liardet, X. Hu, Transition metal oxides as electrocatalysts for the oxygen evolution reaction in alkaline solutions: An application-inspired renaissance, J. Am. Chem. Soc. 7748–7759 (2018).

[11] W. Tong, M. Forster, F. Dionigi, S. Dresp, R. Sadeghi Erami, P. Strasser, A.J. Cowan, P. Farràs, Electrolysis of low-grade and saline surface water, Nat. Energy. 5 (5) (2020) 367–377.

[12] S. Dresp, F. Dionigi, M. Klingenhof, P. Strasser, Direct electrolytic splitting of seawater: Opportunities and challenges, ACS Energy Lett. 4 (4) (2019) 933–942.

[13] H. Abdelaal, I. Hussein, Parametric study for saline water electrolysis: Part I-hydrogen production, Int. J. Hydrogen Energy. 18 (6) (1993) 485–489.

[14] Y. Huang, L. Hu, R. Liu, Y. Hu, T. Xiong, W. Qiu, M.S. Jie, T. Balogun, A. Pan, Y. Tong, Nitrogen treatment generates tunable nanohybridization of Ni5P4 nanosheets with nickel hydr(oxy)oxides for efficient hydrogen production in alkaline, seawater and acidic media, Appl. Catal. B Environ. 251 (2019) 181–194.

[15] J. Bennett, Electrodes for generation of hydrogen and oxygen from seawater, Int. J. Hydrogen Energy. 5 (4) (1980) 401–408.

[16] B.o. You, Y. Sun, Innovative Strategies for Electrocatalytic Water Splitting, Acc. Chem. Res. 51 (7) (2018) 1571–1580.

[17] T. Hisatomi, J. Kubota, K. Domen, Recent advances in semiconductors for photocatalytic and photoelectrochemical water splitting, Chem. Soc. Rev. 43 (22) (2014) 7520–7535.

[18] Z. Zeng, K.C. Chang, J. Kubal, N.M. Markovic, J. Greeley, Stabilization of ultrathin (hydroxy)oxide films on transition metal substrates for electrochemical energy conversion, Nat. Energy. 2 (2017) 1–9.

[19] J.R. McKone, S.C. Marinescu, B.S. Brunschwig, J.R. Winkler, H.B. Gray, Earth-abundant hydrogen evolution electrocatalysts, Chem. Sci. 5 (3) (2014) 865–878.

[20] W. Luc, F. Jiao, Nanoporous Metals as Electrocatalysts: State-of-the-Art, Opportunities, and Challenges, ACS Catal. 7 (2017) 5856–5865.

[21] M. Nanocatalysts, T.F. Jaramillo, K.P. Jørgensen, J. Bonde, J.H. Nielsen, S. Horch, I. Chorkendorff, Identification of Active Edge Sites for Electrochemical H_2 Evolution from MoS2 Nanocatalysts, Science. 317 (2007) 100–102.

[22] R. Ge, J. Huo, T. Liao, Y. Liu, M. Zhu, Y. Li, J. Zhang, W. Li, Hierarchical molybdenum phosphide coupled with carbon as a whole pH-range electrocatalyst for hydrogen evolution reaction, Appl. Catal. B Environ. 260 (2020) 118196–118206.

[23] X. Zhao, Z. Zhang, X. Cao, J. Hu, X. Wu, A.Y.R. Ng, G.P. Lu, Z. Chen, Elucidating the sources of activity and stability of FeP electrocatalyst for hydrogen evolution reactions in acidic and alkaline media, Appl. Catal. B Environ. 260 (2020) 118156–118163.

[24] C.C.L. McCrory, S. Jung, I.M. Ferrer, S.M. Chatman, J.C. Peters, T.F. Jaramillo, Benchmarking Hydrogen Evolving Reaction and Oxygen Evolving Reaction Electrocatalysts for Solar Water Splitting Devices, J. Am. Chem. Soc. 137 (13) (2015) 4347–4357.

[25] V. Vij, S. Sultan, A.M. Harzandi, A. Meena, J.N. Tiwari, W.G. Lee, T. Yoon, K. S. Kim, Nickel-based electrocatalysts for energy-related applications: Oxygen reduction, oxygen evolution, and hydrogen evolution reactions, ACS Catal. 7 (2017) 7196–7225.

[26] X. Liu, K. Ni, C. Niu, R. Guo, W. Xi, Z. Wang, J. Meng, J. Li, Y. Zhu, P. Wu, Q.i. Li, J. Luo, X. Wu, L. Mai, Upraising the O 2p Orbital by Integrating Ni with MoO2 for Accelerating Hydrogen Evolution Kinetics, ACS Catal. 9 (3) (2019) 2275–2285.

[27] J. Huang, J. Han, T. Wu, K. Feng, T. Yao, X. Wang, S. Liu, J. Zhong, Z. Zhang, Y. Zhang, B.o. Song, Boosting Hydrogen Transfer during Volmer Reaction at Oxides/Metal Nanocomposites for Efficient Alkaline Hydrogen Evolution, ACS Energy Lett. 4 (12) (2019) 3002–3010.

[28] M. Fang, W. Gao, G. Dong, Z. Xia, SenPo Yip, Y. Qin, Y. Qu, J.C. Ho, Hierarchical NiMo-based 3D electrocatalysts for highly-efficient hydrogen evolution in alkaline conditions, Nano Energy. 27 (2016) 247–254.

[29] T. Liu, H. Liu, X. Wu, Y. Niu, B. Feng, W. Li, W. Hu, C.M. Li, Molybdenum carbide/phosphide hybrid nanoparticles embedded P, N co-doped carbon nanofibers for highly efficient hydrogen production in acidic, alkaline solution and seawater, Electrochim. Acta. 281 (2018) 710–716.

[30] Y.-Y. Ma, C.-X. Wu, X.-J. Feng, H.-Q. Tan, L.-K. Yan, Y. Liu, Z.-H. Kang, E.-B. Wang, Y.-G. Li, Highly efficient hydrogen evolution from seawater by a low-cost and stable CoMoP@C electrocatalyst superior to Pt/C, Energy Environ. Sci. 10 (3) (2017) 788–798.

[31] P. Kumar, E. Vahidzadeh, U.K. Thakur, P. Kar, K.M. Alam, A. Goswami, N. Mahdi, K. Cui, G.M. Bernard, V.K. Michaelis, K. Shankar, C_3N_5: A Low Bandgap Semiconductor Containing an Azo-Linked Carbon Nitride Framework for Photocatalytic, Photovoltaic and Adsorbent Applications, J. Am. Chem. Soc. 141 (2019) 5415–5436.

[32] H. Zhang, Z. Ma, J. Duan, H. Liu, G. Liu, T. Wang, K. Chang, M. Li, L. Shi, X. Meng, K. Wu, J. Ye, Active sites implanted carbon cages in core-shell architecture: Highly active and durable electrocatalyst for hydrogen evolution reaction, ACS Nano. 10 (2016) 684–694.

[33] P. Giannozzi, O. Andreussi, T. Brumme, O. Bunau, M. Buongiorno Nardelli, M. Calandra, R. Car, C. Cavazzoni, D. Ceresoli, M. Cococcioni, N. Colonna, I. Carnimeo, A. Dal Corso, S. de Gironcoli, P. Delugas, R.A. DiStasio, A. Ferretti, A. Floris, G. Fratesi, G. Fugallo, R. Gebauer, U. Gerstmann, F. Giustino, T. Gorni, J. Jia, M. Kawamura, H.-Y. Ko, A. Kokalj, E. Küçükbenli, M. Lazzeri, M. Marsili, N. Marzari, F. Mauri, N.L. Nguyen, H.-V. Nguyen, A. Otero-de-la-Roza, L. Paulatto, S. Poncé, D. Rocca, R. Sabatini, B. Santra, M. Schlipf, A.P. Seitsonen, A. Smogunov, I. Timrov, T. Thonhauser, P. Umari, N. Vast, X. Wu, S. Baroni, Advanced capabilities for materials modelling with Quantum ESPRESSO, J. Phys. Condens. Matter. 29 (46) (2017) 465901, https://doi.org/10.1088/1361-648X/aa8f79.

[34] P. Giannozzi, S. Baroni, N. Bonini, M. Calandra, R. Car, C. Cavazzoni, D. Ceresoli, G.L. Chiarotti, M. Cococcioni, I. Dabo, A. Dal Corso, S. De Gironcoli, S. Fabris, G. Fratesi, R. Gebauer, U. Gerstmann, C. Gougoussis, A. Kokalj, M. Lazzeri, L. Martin-Samos, N. Marzari, F. Mauri, R. Mazzarello, S. Paolini, A. Pasquarello, L. Paulatto, C. Sbraccia, S. Scandolo, G. Sclauzero, A.P. Seitsonen, A. Smogunov, P. Umari, R.M. Wentzcovitch, QUANTUM ESPRESSO: A modular and open-source software project for quantum simulations of materials, J. Phys. Condens. Matter. 21 (2009) 395502–395521.

[35] J.P. Perdew, K. Burke, M. Ernzerhof, Generalized gradient approximation made simple, Phys. Rev. Lett. 77 (18) (1996) 3865–3868.

[36] S. Grimme, J. Antony, S. Ehrlich, H. Krieg, A consistent and accurate ab initio parametrization of density functional dispersion correction (DFT-D) for the 94 elements H-Pu, J. Chem. Phys. 132 (15) (2010) 154104, https://doi.org/10.1063/1.3382344.

[37] J.M. Smith, S.P. Jones, L.D. White, Soft self-consistent pseudopotentials in a generalized eigenvalue formalism, Phys. Rev. B. 41 (1990) 7892–7895.

[38] K. Lejaeghere, G. Bihlmayer, T. Björkman, P. Blaha, S. Blügel, V. Blum, D. Caliste, I. E. Castelli, S.J. Clark, A. Dal Corso, S. de Gironcoli, T. Deutsch, J.K. Dewhurst, I. Di Marco, C. Draxl, M. Dułak, O. Eriksson, J.A. Flores-Livas, K.F. Garrity, L. Genovese, P. Giannozzi, M. Giantomassi, S. Goedecker, X. Gonze, O. Grånäs, E.K.U. Gross,

A. Gulans, F. Gygi, D.R. Hamann, P.J. Hasnip, N.A.W. Holzwarth, D. Iuşan, D. B. Jochym, F. Jollet, D. Jones, G. Kresse, K. Koepernik, E. Küçükbenli, Y. O. Kvashnin, I.L.M. Locht, S. Lubeck, M. Marsman, N. Marzari, U. Nitzsche, L. Nordström, T. Ozaki, L. Paulatto, C.J. Pickard, W. Poelmans, M.I.J. Probert, K. Refson, M. Richter, G.-M. Rignanese, S. Saha, M. Scheffler, M. Schlipf, K. Schwarz, S. Sharma, F. Tavazza, P. Thunström, A. Tkatchenko, M. Torrent, D. Vanderbilt, M.J. van Setten, V. Van Speybroeck, J.M. Wills, J.R. Yates, G.-X. Zhang, S. Cottenier, Reproducibility in density functional theory calculations of solids, Science. 351 (6280) (2016).

[39] A.A. Peterson, F. Abild-Pedersen, F. Studt, J. Rossmeisl, J.K. Nørskov, How copper catalyzes the electroreduction of carbon dioxide into hydrocarbon fuels, Energy Environ. Sci. 3 (9) (2010) 1311, https://doi.org/10.1039/c0ee00071j.

[40] D. Strmcnik, P.P. Lopes, B. Genorio, V.R. Stamenkovic, N.M. Markovic, Design principles for hydrogen evolution reaction catalyst materials, Nano Energy. 29 (2016) 29–36.

[41] B. Zhang, J. Liu, J. Wang, Y. Ruan, X. Ji, K. Xu, C. Chen, H. Wan, L. Miao, J. Jiang, Interface engineering: The $Ni(OH)_2/MoS_2$ heterostructure for highly efficient alkaline hydrogen evolution, Nano Energy. 37 (2017) 74–80.

[42] G. Henkelman, B.P. Uberuaga, H. Jónsson, Climbing image nudged elastic band method for finding saddle points and minimum energy paths, J. Chem. Phys. 113 (2000) 9901–9904.

[43] H. Jónsson, G. Mills, K. W. Jacobsen, "Nudged Elastic Band Method for Finding Minimum Energy Paths of Transitions," in Classical and Quantum Dynamics in Condensed Phase Simulations, Ed. B. J. Berne, G. Ciccotti and D. F. Coker (World Scientific, 1998), page 385.

[44] D.A. Köse, H. Necefoğlu, Synthesis and characterization of bis(nicotinamide) m-hydroxybenzoate complexes of Co(II), Ni(II), Cu(II) and Zn(II), J. Therm. Anal. Calorim. 93 (2) (2008) 509–514.

[45] H. Wu, K. Lian, The Development of Pseudocapacitive Molybdenum Oxynitride Electrodes for Supercapacitors, ECS Trans. 58 (25) (2014) 67–75.

[46] X. Bu, R. Wei, W. Gao, C. Lan, J.C. Ho, A unique sandwich structure of a $CoMnP/Ni_2 P/NiFe$ electrocatalyst for highly efficient overall water splitting, J. Mater. Chem. A. 7 (19) (2019) 12325–12332.

[47] Q. Yang, Q. Xu, H.-L. Jiang, Metal–organic frameworks meet metal nanoparticles: synergistic effect for enhanced catalysis, Chem. Soc. Rev. 46 (2017) 4774–4808.

[48] W. Li, F. Li, X. Wang, Y.u. Tang, Y. Yang, W. Gao, R. Li, A facile lyophilization synthesis of $MoS_2QDs@graphene$ as a highly active electrocatalyst for hydrogen evolution reaction, Appl. Surf. Sci. 401 (2017) 190–197.

[49] W. Yuan, S. Wang, Y. Ma, Y. Qiu, Y. An, L. Cheng, Interfacial Engineering of Cobalt Nitrides and Mesoporous Nitrogen-Doped Carbon: Toward Efficient Overall Water-Splitting Activity with Enhanced Charge-Transfer Efficiency, ACS Energy Lett. 5 (2020) 692–700.

[50] Z. Cai, X. Bu, P. Wang, J.C. Ho, J. Yang, X. Wang, Recent advances in layered double hydroxide electrocatalysts for the oxygen evolution reaction, J. Mater. Chem. A. 7 (10) (2019) 5069–5089.

[51] J. Zhang, W. Xiao, P. Xi, S. Xi, Y. Du, D. Gao, J. Ding, Activating and Optimizing Activity of CoS_2 for Hydrogen Evolution Reaction through the Synergic Effect of N Dopants and S Vacancies, ACS Energy Lett. 2 (5) (2017) 1022–1028.

[52] R. Wei, M. Fang, G. Dong, C. Lan, L. Shu, H. Zhang, X. Bu, J.C. Ho, High-Index Faceted Porous Co_3O_4 Nanosheets with Oxygen Vacancies for Highly Efficient Water Oxidation, ACS Appl. Mater. Interfaces. 10 (8) (2018) 7079–7086.

[53] X. Liang, R. Dong, D. Li, X. Bu, F. Li, L. Shu, R. Wei, J.C. Ho, Coupling of Nickel Boride and $Ni(OH)_2$ Nanosheets with Hierarchical Interconnected Conductive Porous Structure Synergizes the Oxygen Evolution Reaction, ChemCatChem. 10 (20) (2018) 4555–4561.

[54] S. Zhu, X. Qin, F. Xiao, S. Yang, Y. Xu, Z. Tan, J. Li, J. Yan, Q. Chen, M. Chen, M. Shao, The role of ruthenium in improving the kinetics of hydrogen oxidation and evolution reactions of platinum, Nat. Catal. 4 (8) (2021) 711–718.

[55] R. Zhang, Z. Wei, G. Ye, G. Chen, J. Miao, X. Zhou, X. Zhu, X. Cao, X. Sun, "d-Electron Complementation" Induced V-Co Phosphide for Efficient Overall Water Splitting, Adv. Energy Mater. 11 (38) (2021) 2101758, https://doi.org/10.1002/aenm.v11.3810.1002/aenm.202101758.

[56] Q. Zhang, W. Xiao, W.H. Guo, Y.X. Yang, J.L. Lei, H.Q. Luo, N.B. Li, Macroporous Array Induced Multiscale Modulation at the Surface/Interface of $Co(OH)_2/NiMo$ Self-Supporting Electrode for Effective Overall Water Splitting, Adv. Funct. Mater. 31 (33) (2021) 2102117, https://doi.org/10.1002/adfm.v31.3310.1002/adfm.202102117.